

OPEN ACCESS

EDITED BY
Daniele Lana,
University of Florence, Italy

REVIEWED BY

Edgar López-López, National Polytechnic Institute of Mexico (CINVESTAV), Mexico Ovais Shafi, Jinnah Sindh Medical University, Pakistan

*CORRESPONDENCE Alexey Rayevsky,

□ rayevsky85@gmail.com

†PRESENT ADDRESS Samofalova Dariia, I.F. Lab, LLC, Life Chemicals Inc., Kyiv, Ukraine

[†]These authors have contributed equally to this work

RECEIVED 25 June 2025 ACCEPTED 19 September 2025 PUBLISHED 07 October 2025

CITATION

Rybachuk O, Rayevsky A, Styhylias M, Samofalova D, Bulgakov E, Platonov M, Blume Y and Karpov P (2025) Computational and experimental identification of putative aTAT1 modulators: implications for nervous system function.

Front. Pharmacol. 16:1654114.
doi: 10.3389/fphar.2025.1654114

COPYRIGHT

© 2025 Rybachuk, Rayevsky, Styhylias, Samofalova, Bulgakov, Platonov, Blume and Karpov. This is an open-access article distributed under the terms of the Creative Commons Attribution License (CC BY). The use, distribution or reproduction in other forums is permitted, provided the original author(s) and the copyright owner(s) are credited and that the original publication in this journal is cited, in accordance with accepted academic practice. No use, distribution or reproduction is permitted which does not comply with these terms

Oksana Rybachuk^{1,2‡}, Alexey Rayevsky^{3,4*‡}, Mariia Styhylias³, Dariia Samofalova^{3†}, Elijah Bulgakov^{3,5}, Maxym Platonov^{4,5}, Yaroslav Blume³ and Pavel Karpov^{3‡}

¹Bogomoletz Institute of Physiology, National Academy of Sciences of Ukraine, Kyiv, Ukraine, ²Institute of Genetic and Regenerative Medicine, M. D. Strazhesko National Scientific Center of Cardiology, Clinical and Regenerative Medicine, National Academy of Medical Sciences of Ukraine, Kyiv, Ukraine, ³Institute of Food Biotechnology and Genomics, National Academy of Sciences of Ukraine, Kyiv, Ukraine, ⁴Institute of Molecular Biology and Genetics, National Academy of Sciences of Ukraine, Kyiv, Ukraine, ⁵Enamine Ltd., Kyiv, Ukraine

Introduction: The project's primary objective is to understand how enzymes responsible for post-translational modifications (PTMs) of microtubule elements influence ion channels in excitatory peripheral nervous system (PNS) cells, and to subsequently identify potential pharmacological agents that can act upon these molecular targets. Having identified HDAC6 and α TAT1 as the most relevant proteins for further study, we focused on α TAT1. α TAT1 is the sole mammalian enzyme known to acetylate microtubules, a process associated with regulating their dynamics and protecting long-lived microtubules from mechanical stress. Additionally, α TAT1 plays a role in nuclear processes such as DNA replication, cell migration, and axonal transport. Given the importance of α TAT1 in cytoskeletal homeostasis and the lack of known effectors, our research focused on this enzyme.

Methods: We designed a corresponding pharmacophore model hypothesis of ligand-dependent inhibition for $\alpha TAT1$ and performed search for potential $\alpha TAT1$ modulators using molecular interaction analysis and existing crystal structures. Confocal microscopy was used to assess cytoskeletal changes in a neural stem cell line following experimental treatment.

Results: The activity of identified hits was confirmed via confocal microscopy. This allowed for further tuning of our screening models and generation of novel subsets of compounds.

KEYWORDS

αTAT1, microtubule, docking, pharmacophore, neural stem cells

Introduction

Microtubules (MTs), the primary components of the eukaryotic cytoskeleton, are formed by the polymerization of α - and β -tubulin heterodimers. The diverse tubulin isotypes and a variety of post-translational modifications (PTMs) tightly regulate MT properties and functions, giving rise to the "tubulin code" (Janke and Magiera, 2020). These PTMs can be reversible, such as phosphorylation, or likely irreversible, for instance, nitration (Juzzolino et al., 2024; Sánchez-Fernández et al., 2023).

Phosphorylation is considered the most common and wellstudied of all known microtubule (MT) post-translational modifications (PTMs) (Janke and Magiera, 2020; Fu et al., 2015; Samofalova et al., 2019). As a result, tubulin phosphorylation can almost completely inhibit microtubule polymerization (U et al., 2020). In addition to phosphorylation, acetylation is a critical tubulin PTM that influences microtubule polymerization levels and has an indirect impact on autophagy processes (Coombes et al., 2020; Aguilar et al., 2014; Wong et al., 2014). This effect was subsequently confirmed experimentally, demonstrating significant alterations in tubulin heterodimer stability (Sardar et al., 2012). This finding strongly supports the link between α-tubulin acetylation, the formation of stable microtubules, and their protection from mechanical ageing (Goswami et al., 2010). Although a major part of the components involved in this process has already been described in detail, the mechanism of microtubule stabilization due to this modification has not yet been elucidated and requires further research (Dybkova et al., 2014; Rayevsky et al., 2023; Rayevsky et al., 2025; Rayevsky et al., 2019).

Rearrangements within α-tubulin's secondary structure are crucial for the dynamic reorganization of microtubules. Numerous studies have highlighted the role of α-tubulin N-acetyltransferase (\alpha TAT1), an enzyme typically found in animal cells, in acetylating α-tubulin at the Lys40 position (Wong et al., 2014; Rayevsky, et al., 2025; Huang et al., 2017). The reversible process is provided by HDA6/12 deacetylases (U et al., 2020; Ferreira de Freitas et al., 2018; Stykhylias et al., 2024). Adding to the complexity, aTAT1 acetylates Lys40 and Lys60 on the luminal side of microtubules, raising the question of how the enzyme accesses this site (Rakhshani et al., 2019; Liu et al., 2015). Studies have demonstrated that induced dysfunction of aTAT1 results in a substantial loss of mechanical sensitivity in peripheral nervous system cells. Intriguingly, despite the significant evolutionary conservation of tubulins and confirmed microtubule acetylation in plants, neither aTAT1 nor proteins exhibiting comparable predicted function have been identified in the plant kingdom (Friedmann et al., 2012). At the same time, MYST and p300-like enzymes can acetylate plant proteins (Han et al., 2007; Rayevsky et al., 2016).

Therefore, lysine acetylation is a key post-translational modification (PTM) governing microtubule structure and interactions with tau and other microtubule-associated proteins involved in Alzheimer's disease. However, αTAT1's role extends beyond microtubules; it can participate in multi-protein complexes and modify unidentified substrates, crucial in DNA replication and repair (Wu et al., 2018). αTAT1 exhibited non-enzymatic activities in cell migration, non-axonal intracellular transport and nonneuronal diseases (Topalidou et al., 2012; Dan et al., 2018). Also, too little is known about the significance of ATAT1 acetyltransferase activity in cancer development and any details of the underlying process. Due to the undoubted and important role of the enzyme and the lack of published data on modulators of aTAT1 activity, this area of research is promising in terms of fundamental knowledge and practical application of the results. Our task was to develop models for searching commercial databases and further confirm the activity of hits by analyzing the state of the cytoskeleton of neuronal cells using confocal microscopy.

Methods and materials

Molecular docking and pharmacophore search

The human $\alpha TAT1$ sequence was taken from the UniProtKB database (Q5SQI0) and analyzed using the internal services in an attempt to find any similar proteins or even complexes in the Protein Data Bank (UniProt Consortium, 2025; Zardecki et al., 2022). Since only the catalytic domains of the target protein were found, we used two complexes with acetyl-coenzyme A and a bisubstrate analogue (PDB ID: 4G4 and 4PK3) as a starting point for the binding mode assessment. To describe the extended and vaste binding pocket of 4PK3, we employed both structural methods (PyMOL plugin, CavitOmiX, PLIP) and a ligand-based site mapping method (LigPlot with LigandScout 4.4) (Wolber et al., 2006; Wolber and Langer, 2005; La et al., 2011; Adasme et al., 2021). Consequently, we mapped all potential ligand-protein interactions within the binding cavity, including donors and acceptors, to determine their reactivity and identify crucial residues and atoms.

The centroids for subsequent descriptors were then determined based on the coordinates of CavitOmiX innophores that filled the pocket, selected according to the canonical distances of their respective interaction types. The remaining pseudoatoms of the cloud were removed. The resulting structure (protein fragment + remaining probes) was saved in the *.pdb format and using the built-in tool final refinement of the model was completed in the LigandScout program.

An important aspect was that LigandScout allowed the built model to be saved in the *.pmz format, which is compatible with the Pharmit online service (https://pharmit.csb.pitt.edu/search.html) and connected to the Enamine compound library, which was the specific library that needed to be screened. During the final system setup, the properties of the features were defined as follows: their diameters were set (R = 1), interaction vectors were adjusted according to the donors and acceptors of the target site, as well as according to the centroids of cyclic fragments of aromatic amino acids, allowing for parallel/perpendicular stacking $(\pi - \pi)$. For cyclic interactions, the features allowed for π - π and/or hydrophobic interactions. Ultimately, the ligand docking model in the binding site was constructed based on three anchors formed by assigning hydrophobic regions, four hydrogen-bonding atoms, and one steric constraint (corresponding to a negatively charged group) in the region of the acetyl and diphosphate sites (one interaction with R158 or K165 in the acetyl site is required). Screening results were ranked according to their "Score." The Score threshold was defined as the minimum Score value found in the control group compounds.

The control group of compounds was additionally processed with a molecular docking procedure performed in the CCDC Gold 5.3 program (www.ccdc.cam.ac.uk), which works based on a genetic algorithm for creating new ligand conformations. Hydrogens have been added to the protein structure by *Hermes*. Experimentally solved conformation of the protonated ligand was used to define interactions and binding area. Radius of the binding site area (5Å) for the docking was defined selecting the phosphate group of the substrate in the crystal structure (4PK3). Initially we supposed to apply H-bond constraints to the backbone atoms of amino acids Ile126, Gly134, Gly136, but shifted our attention at the interactions

with amino acids Arg132 and His170, which were set as H-bond constraints. Residue Gln131 was set as flexible to increase as we suggested it can find more favorable interaction with novel ligands. Then we defined hydrophobic area between Phe124 and Phe166 as a hydrophobic region constrain. The docking process utilized standard parameters, including a population size of 100, a sample size of 1.1, 10 islands, and 100,000 genetic operations. Docking maps were created in a rectangular box with a 0.5 Å grid spacing, centered on the predicted ligand binding site. The fitness function settings included a ChemPLP, as a first sieve to pass with further re-scoring by ASP function (the Astex Statistical Potential). Finally, the outcome of screened compounds was analyzed with Datawarrior to predict its ADME parameters (López-López et al., 2019). All the computational procedures were utilised in our virtual laboratory, CSLabGrid (Karpov et al., 2015; Karpov et al., 2016).

Isolation of the neural stem cells and viability assay

Animals were used by the protocols approved by the Animal Care and Use Committee at Bogomoletz Institute of Physiology (Kyiv, Ukraine) and the Law of Ukraine on the protection of experimental animals (N3447-IV, 21.02.2006). The method of isolation we described previously (Rybachuk et al., 2019). Briefly, hippocampal NSCs from 16-17 dpc FVB-wt mouse embryos (n = 12) were mechanically dissociated in Neurobasal medium (Gibco, United States) under aseptic conditions. The isolated cell suspension was filtered using a 40 µm nylon cell strainer. (Falcon, United States). The NSPC fraction was purified by centrifugation in a 22% Percoll density gradient at 450 g for 10 min (GE Healthcare BioScience, Sweden). Cell viability was determined by flow cytometry based on 7-aminoactinomycin D (7-AAD) incorporation and analyzed using a BD FACSAria cell sorter (Becton Dickinson, United States) and BD FACSDiva software version 6.2.1 (Becton Dickinson, United States).

Culturing of neural stem cells in the medium supplemented with different compounds (C1, C2, C3, C4, and C5)

NSCs were plated on Matrigel-coated coverslips (BD Biosciences, UK) at a density of 5×10^4 cells per well in a 24-well plate and incubated under standard culture conditions (5% $\rm CO_2$, 37 °C) for 48 h. The standard culture medium was Neurobasal medium (Gibco, United States) supplemented with 20 ng/mL bFGF (Sigma, United States), 2% B27 supplement (Invitrogen, United States), 1 mM sodium pyruvate (Invitrogen, United States), 1 mM N-acetyl-L-cysteine (Sigma, United States), 1% L-glutamine (HyClone, United States) and 1% penicillin-streptomycin (Invitrogen, United States).

After 48 h, NSCs were divided into 22 experimental groups and cultured for another 48 h: (a) standard culture medium; (b) standard culture medium + 10 μ M C1; (c) standard culture medium + 100 μ M C1; (d) standard culture medium + 10 μ M C2; (e) standard culture medium + 100 μ M C3; (g) standard culture medium + 100 μ M C3; (h) standard culture

medium + 10 μ M C4; (i) standard culture medium + 100 μ M C4; (j) standard culture medium + 10 μ M C5; (k) standard culture medium + 100 μ M C5; (L) standard culture medium deprived of bFGF; (m) standard culture medium deprived of bFGF + 10 μ M C1; (n) standard culture medium deprived of bFGF + 100 μ M C1; (o) standard culture medium deprived of bFGF + 100 μ M C2; (p) standard culture medium deprived of bFGF + 100 μ M C2; (q) standard culture medium deprived of bFGF + 100 μ M C3; (r) standard culture medium deprived of bFGF + 100 μ M C3; (s) standard culture medium deprived of bFGF + 100 μ M C4; (t) standard culture medium deprived of bFGF + 100 μ M C4; (u) standard culture medium deprived of bFGF + 100 μ M C5; (v) standard culture medium deprived of bFGF + 100 μ M C5; (v) standard culture medium deprived of bFGF + 100 μ M C5.

The total duration of cultivation after seeding was 4 days. The growth of NSCs and the formation of primary adhesive spheres (neurospheres) during cultivation under different conditions were observed using an inverted microscope (Olympus IX 71, Japan) with relief phase contrast.

Immunocytochemical analysis of cultured NSCs

NSC cultures were fixed in 4% paraformaldehyde for 30 min and then washed with a washing buffer (0.1 M PBS). Blocking was carried out for at least 2 h using a blocking solution for permeabilization (washing buffer supplemented with 0.3% Triton X-100 and 0.5% BSA). The NSCs were incubated overnight at 4 $^{\circ}$ C in blocking solution in the presence of primary antibodies at the concentrations recommended by the manufacturer. To identify NSCs, proliferating cells and differentiated NSCs into neurons, double immunostaining was performed using antibodies against Nestin (1:100, Santa Cruz Biotecnology, United States), Ki-67 (1: 200, Abcam, UK), α -tubulin (1:200, Abcam, UK), β (III)-tubulin (1:700, Sigma, Germany) and MAP-2 (1:2000, Abcam, UK). Nestin expression was adopted as a marker for neural stem and precursor cells (Jan and Kotov, 2007; Xiong et al., 2014); β -tubulin (III) is a specific marker for neuronal lineages (Xiong et al., 2014).

After that, the cells were washed with the washing buffer 3 times for 15 min and then incubated in the presence of secondary antibodies for at least 2 h at room temperature. Secondary antibodies were: anti-chicken Alexa Fluor 488 (1:1000, Invitrogen, United States), anti-mouse Alexa Fluor 555 (1:1000, Invitrogen, United States) and anti-rabbit Alexa Fluor 647 (1:1000, Invitrogen, United States). Images were taken with a laser scanning confocal microscope FluoViewTMFV1000 (Olympus, Japan).

Statistical analysis

Statistical analyses were performed using statistical software (version 5, StatSoft, Tulsa). The results are presented as mean \pm standard error of the mean (SEM). Chemical effects on cells were determined using a one-way analysis of variance (ANOVA) with Tukey post hoc HSD. The Kruskal-Wallis test was applied to compare the number of formed primary neurospheres under different cultivation conditions. The difference between means was considered significant at P < 0.05.

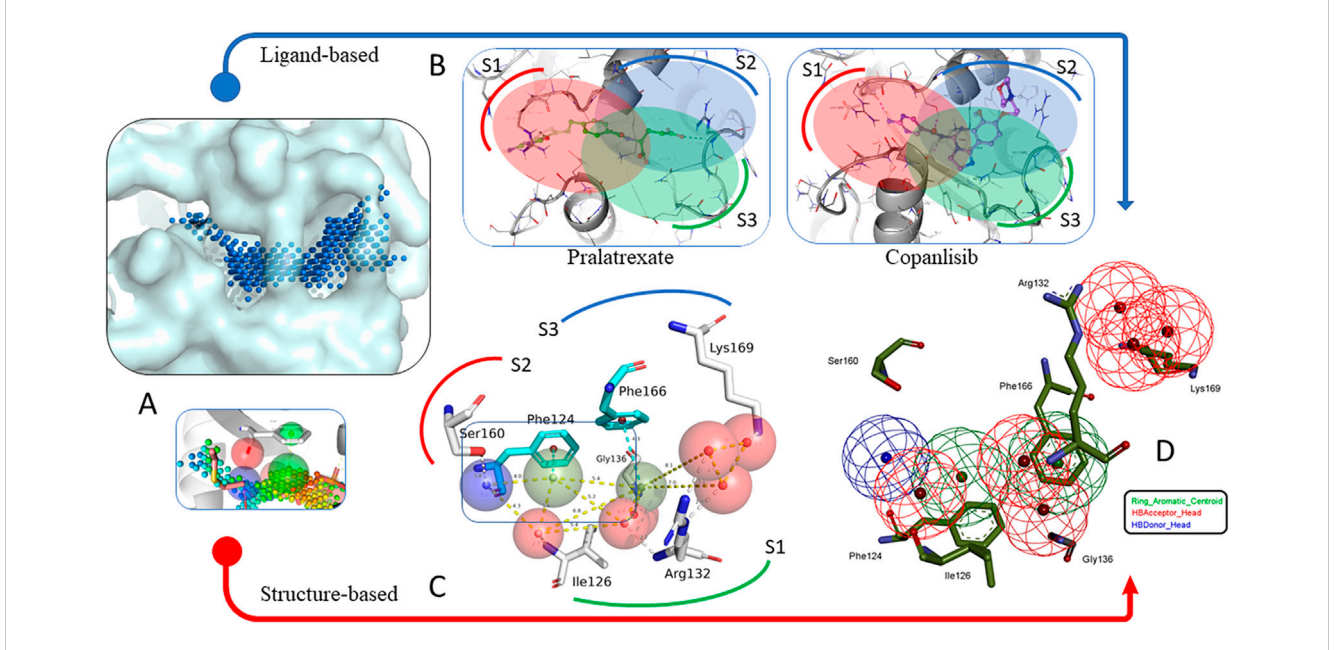


FIGURE 1
Two strategies were developed for the fine screening model generation. (A) Binding site mapping with ionophores (charged probes). Coloring scheme reflects positions of hydrogen bond donors (blue) and acceptors (red), as well as positions of possible cyclic fragments (green). (B) Results of molecular docking for the best of potential aTAT effectors proposed by Hsu et al., 2021. The outcome didn't match the expected poses and interaction distribution (outlined with ovals). (C) Identification of coordinates of the centroids and the volume of individual pharmacophore features (distance-optimal pseudoatoms). (D) The resulting Pharmacophore model used for the screening.

Results

In silico search for potential α TAT effectors

Our preliminary analysis of the α TAT1 structure (4PK3, 1.35 Å) indicated that the active site features an extended, bulky binding pocket. This pocket exhibits minimal ligand-protein adaptation features, likely due to its size and the nature of the substrate. Furthermore, the structure accuracy analysis yielded a global QMEANDisCo index of 0.83 \pm 0.05 (Studer et al., 2020), while Ramachandran plot analysis showed that 94.82% of amino acid residues were in the allowed regions.

We started by testing information about the amino acid composition and surface features of the pocket. The corresponding centroids of the future descriptors were determined among the CavitOmiX innophores that filled the target site pocket and were selected based on the canonical distances of the corresponding interaction types (Figure 1). It was separately found that, taking into account the distance of 4 Å, 6 aromatic amino acids can be involved in ligand binding, namely: Phe124, Tyr125, Phe166, His135, Phe166 and His170.

Further structural analysis of topology and conformational mobility determined that only Phe124 and Phe166 can form potential π - π interactions with the ligand. Thus, a final skeleton of the future pharmacophore was constructed with interaction combinations for future searches. The final model consisted of nine descriptors: 6 hydrogen bond acceptors, 1 hydrogen bond donor, and 2 cyclic fragment markers.

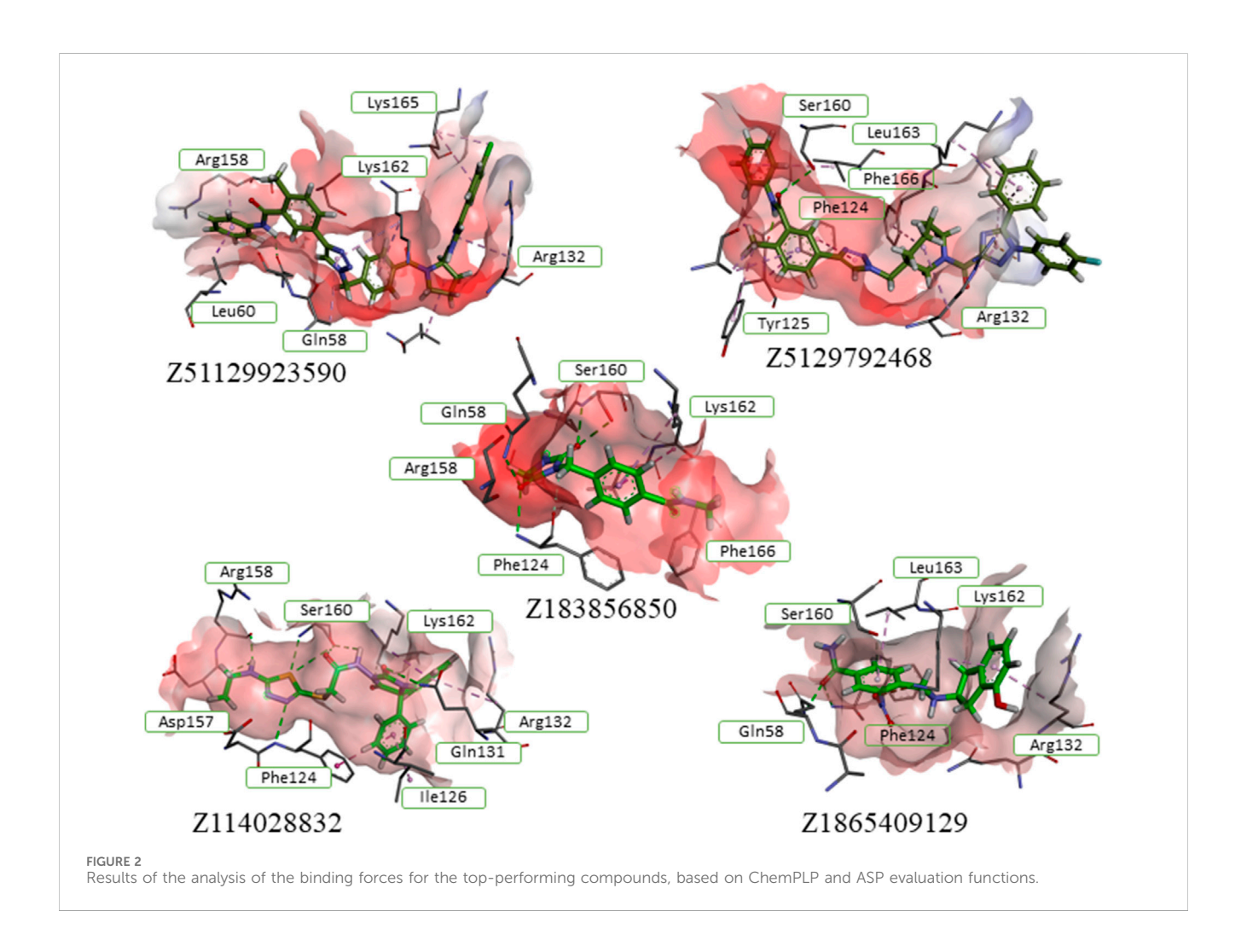
Simultaneously, we conducted docking studies on 10 candidate α TAT1 inhibitors identified by Hsu et al. (2021). According to the CCDC GOLD FitnessScore, 7 of these

compounds exhibited a predicted binding affinity for the target site stronger than that of the natural substrate (acetyl-CoA from 4PK3), yet their binding orientations showed no common trends. At the same time, two compounds (Ceftolozane and Oftasceine) were designated as non-cognate ligands, showing the absence of sufficient interactions. Another, Mangafodipir, was hard to dock and finally interpreted its poses, because of a complex metal-chelating structure (Table 1).

Having analyzed the rates of interactions between different residues and the substrate (crystal complexes of aTAT1) or these 10 compounds, we identified overlapping functional groups in the site of interest. Together with our previous suggestions based on binding site deconstruction, we selected all relevant features in a structure-based protocol to generate target-oriented prediction of potential interactions with novel ligands other than the cognate substrate. From these, we divided the total pool of contacts between the protein and the ligand into three groups of interactions different from those declared by Hsu et al. (2021). First group includes amino acid residues His133, Arg137, Gly134, Gly136, Ser160, Phe124 and Ile126 form hydrogen bonds with keto-, phosphate-, sulfo- and amino groups of the ligand. A second set of residues, Lys162, Asp123, and Tyr125, can interact with the ligand via weak hydrogen bonds involving the thiazole heterocycle and keto groups. As an alternative interaction mode, a third group, Arg132 and Lys169, can form charged contacts with the ligand's heterocycles and phosphate groups. Using the PharmIT web service (https://pharmit.csb.pitt.edu/search.html), a scan of the publicly available online ligand repositories: ChEMBL DB, ZINC DB, and PubChem was performed. Using the full pharmacophore, 10 hits were found in the ChEMBL database and 78 hits in the ZINC database (Figure 2).

TABLE 1 Docking results for the control group and selected screening hits.

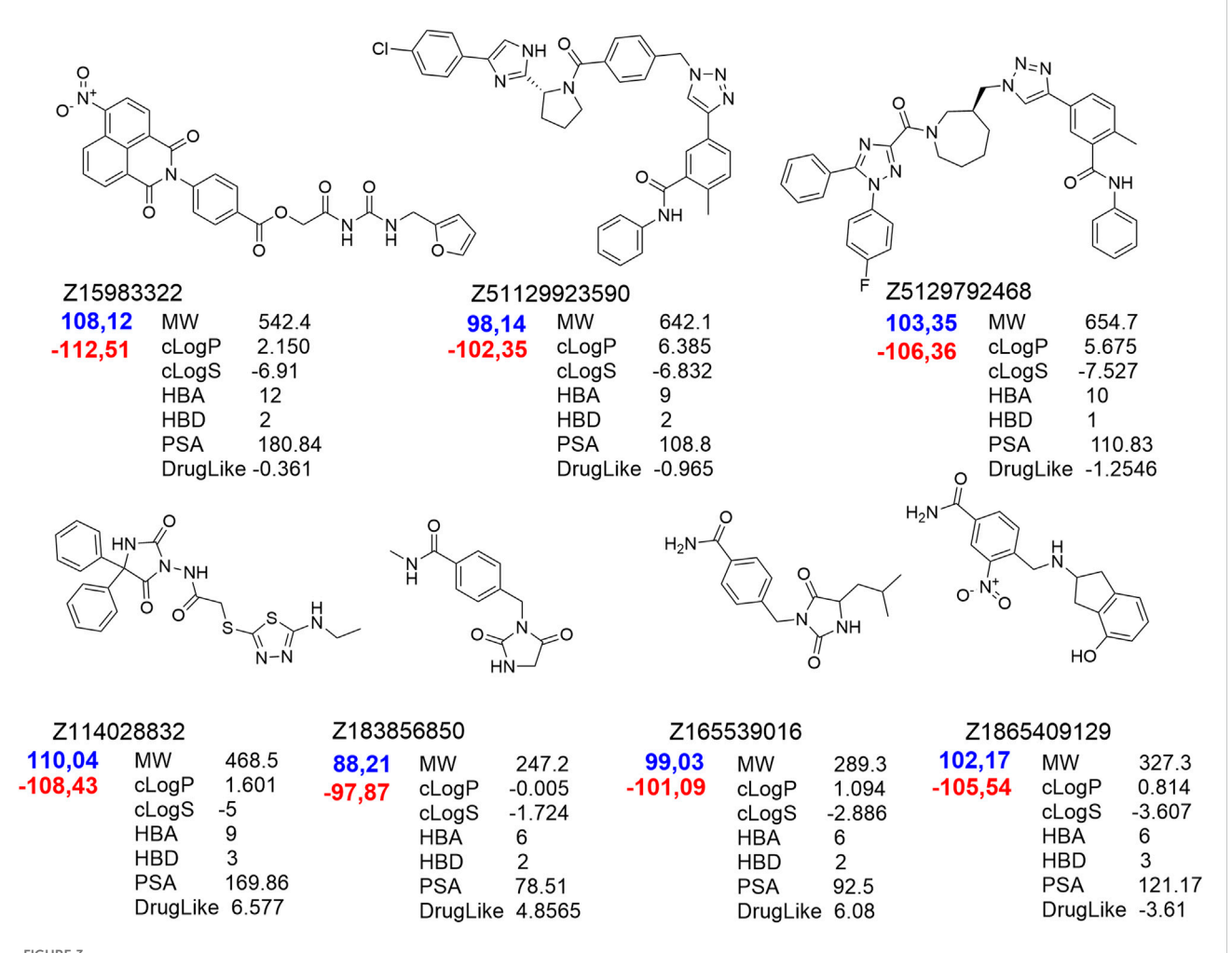
Source	4PK3	Cefonicid	Ceftolozane	Copanlisib	FolicAcid
ChemPLP	49.48	58.53	51.95	57.74	65.86
ASP	-58.04	-61.08	-54.95	-60.37	-68.33
Source	Hesperidin	Pralatrexate	Methotrexate	Oftasceine	Pemetrexed
ChemPLP	58.2	71.65	66.58	-16.58	67.92
ASP	-61.25	-74.17	-69.02	11.49	-70.53



Molecular re-docking in the CCDC GOLD program using a combination of the ChemPLP and ASP fitness functions determined only 7 leaders fitting the target site without clash conflicts and significant indicators of affinity and quality of the complexes. It should be noted that selected ligands had interaction indices higher than that of the best compound from the control group – Pralatrexate (Figure 3). These 7 compounds were analyzed with DataWarrior to predict ADME parameters and show distribution of drug-likeness properties (MW – molecular weight, HBA/HBD – acceptors/donors, cLogP/cLogS – solubilities, PSA – polar surface area). Trying to reach balance between values of drug-likeness, molecular weight and docking scores we selected only five compounds ready to be assessed in cells.

Experimental confirmation of the aTAT1-targeting

According to the results of testing the viability of NSCs, it was found that the percentage of live cells in the suspension was not less than 94.8% \pm 0.3%, which is a high indicator of the viability of freshly isolated NSCs. When culturing NSCs under standard conditions (with the addition of bFGF), the number of cells was 1109.96 \pm 44.82 (n = 47) per mm2, and when 10 μM of C1, C2, C3, C4, and C5 (Z1865409129, Z114028832, Z165539016, Z183856850, and Z15983322, respectively) were added to the culture medium, the number of NSCs significantly decreased to 782.85 \pm 59.77 (n = 16)



Hit compounds from the ZINC DB showed best scores in the final docking of the PharmIT search results. Values of the scoring functions are represented in colors - Score (red labels) and S(PLP) (dark blue labels).

(p < 0.001), 609.12 ± 48.01 (n = 17) (p < 0.001), 852.72 ± 62.01 (n = 17) (p < 0.01) and 300.86 ± 78.28 (n = 15) (p < 0.001) per mm², respectively. (Figures 4a,c,g, 5a) while the addition of the same concentration of C4 did not lead to a significant and reliable change in the number of cells - 943.01 ± 72.14 (n = 18) (Figure 5a)- 943.01 ± 72.14 (n = 18) (Figure 5a). At the same time, increasing the concentration of C1-C5 to 100 μM in the cultivation medium led to significant changes in the number of NSCs, namely, their decrease: 690.56 ± 40.92 (n = 16) (p < 0.001), 919.92 ± 76.04 (n = 17) (p < 0.05), 801.08 ± 65.51 (n = 17) (p < 0.001), 937.21 ± 61.03 (n = 18) (p < 0.05) and 272.83 ± 39.17 (n = 15) (p < 0.001) per mm², respectively (Figures 4e, 5a). It should be noted that the presence of C2 in the culture medium at a concentration of 100 μM contributes to the greater cellularity (p < 0.01) compared to NSCs cultured at a 10 μM concentration of this substance (Figures 4c,e, 5a).

In cultures grown without bFGF, the number of NSCs was 954.06 \pm 38.52 per mm2 (n = 35), a significant decrease compared to control cultures with bFGF (p < 0.01). The addition of 10 μ M of compounds C1, C2, C3, and C5 further significantly reduced the number of NSCs to 603.83 \pm 49.86 (n = 16, p < 0.001), 720.01 \pm 84.21 (n = 15, p < 0.05), 823.74 \pm 42.52 (n = 19, p < 0.05), and 320.17 \pm

 $30.21 \text{ (n = 14, p < 0.001) per mm}^2$, respectively. (Figure 4b, 5b); however, addition of C4 at this concentration significantly increased the number of NSCs to 1224.93 \pm 98.27 (n = 17) (p < 0.05) (Figures 4f, 5b). Adding 100 µM concentrations of C1, C2, and C4 resulted in no significant quantitative changes in the NSC culture: 974.54 \pm $130.51 \text{ (n = 18)}, 859.60 \pm 78.19 \text{ (n = 16)}, 903.59 \pm 55.72 \text{ (n = 18) per}$ mm², respectively (Figures 4d,g,h, 5b). However, when C3 and C5 were added, the number of NSCs under the above cultivation conditions significantly decreased: 770.57 ± 45.07 (n = 17) (p < 0.01) i 212.78 \pm 32.76 (n = 16) (p < 0.001) per mm², respectively (Figure 5b). Intriguingly, in the absence of bFGF, while 10 µM C1 significantly decreased NSC numbers (as shown previously), increasing the C1 concentration to 100 µM resulted in a significant increase (p < 0.05) in cell number compared to the lower dose (Figure 5b). Similarly, in the absence of bFGF, C4 and C5 significantly reduced the number of NSCs (p < 0.01 and p < 0.05, respectively) (Figures 4f,h, 5b). Notably, C5 consistently caused a significant decrease in NSC numbers under all tested conditions (48 h), with only single cells observed in some wells (Figures 4g, 5a,b). These findings collectively indicate a cytotoxic effect of C5 on NSCs.

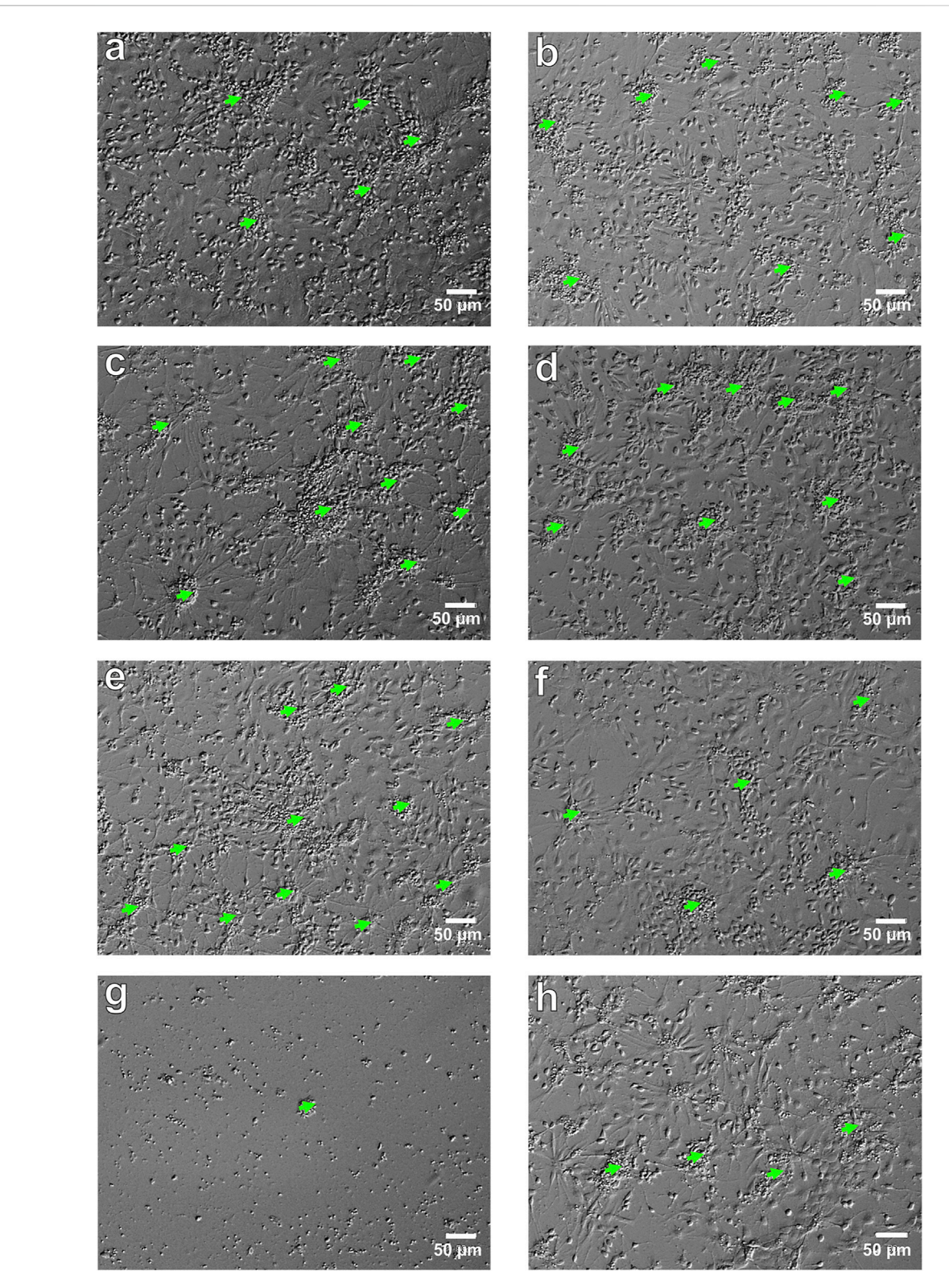
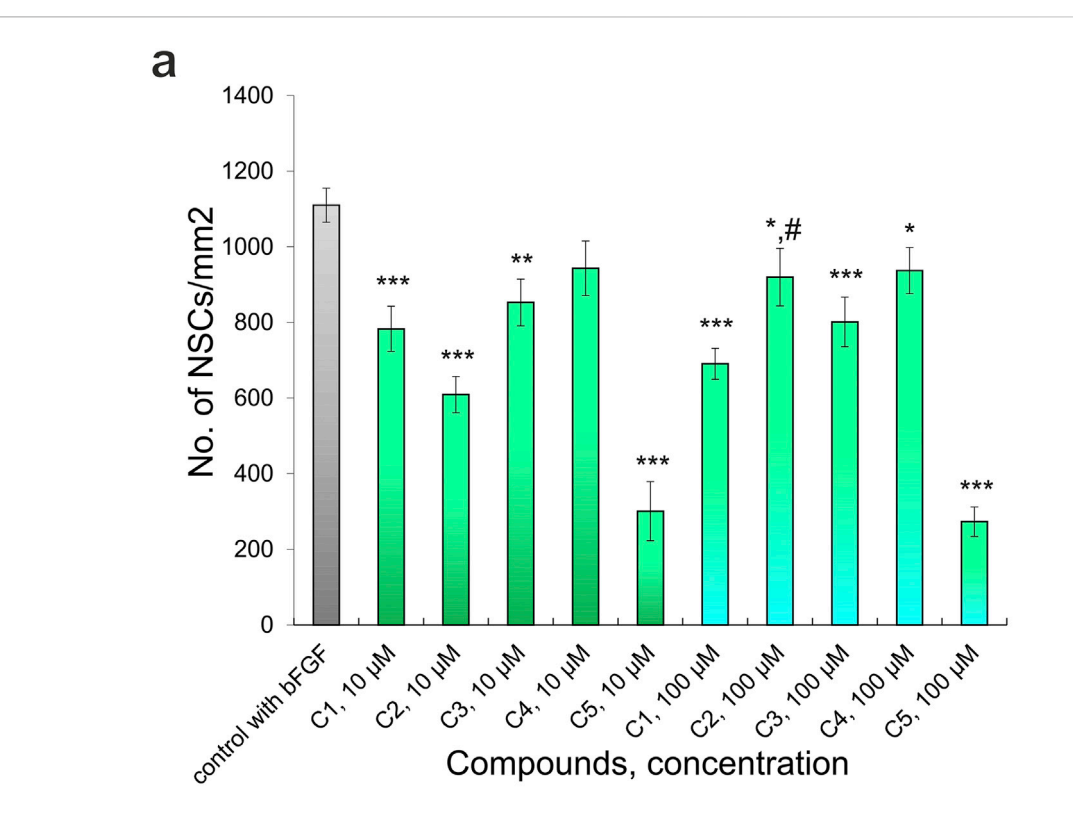


FIGURE 4

NSCs in vitro. Micrograph of NSCs in various culture conditions: (a) control, NSCs culturing with bFGF (NSCs + bFGF); (b) control, NSCs culturing without bFGF (NSCs); (c) NSCs + bFGF+10 µM C2 (48 h); (d) NSCs+100 µM C2 (48 h); (e) NSCs + bFGF+100 µM C2 (48 h); (f) NSCs+100 µM C4 (48 h). Relief contrast inverted microscope; light green arrows—primary adhesive neurospheres; scale bars = 50 µm.



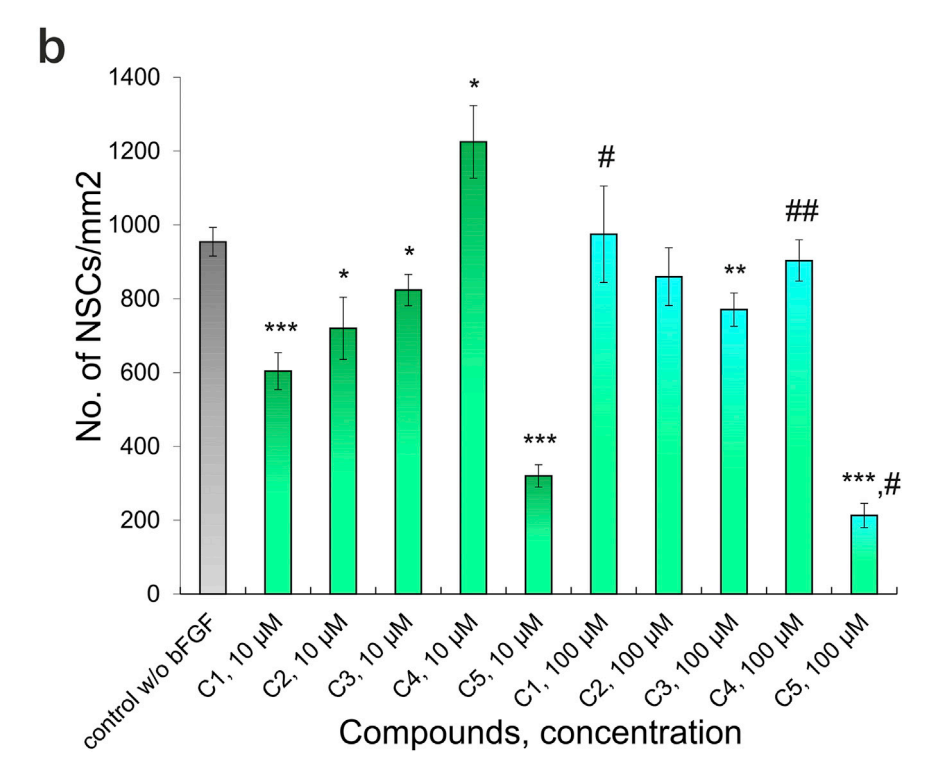


FIGURE 5 Effect of different concentrations of Compounds (C1-C5) on the NSCs (48 h culturing): (a) culturing with added bFGF, (b) culturing without added bFGF. P-values derived from the Student's two-tailed t-test, the results are shown as mean \pm SEM; *p < 0.05, **p < 0.01 and ***p < 0.001 versus control with bFGF (a) and versus control without bFGF (b); #p < 0.05 and ##p < 0.01 versus different concentrations of one's compound.

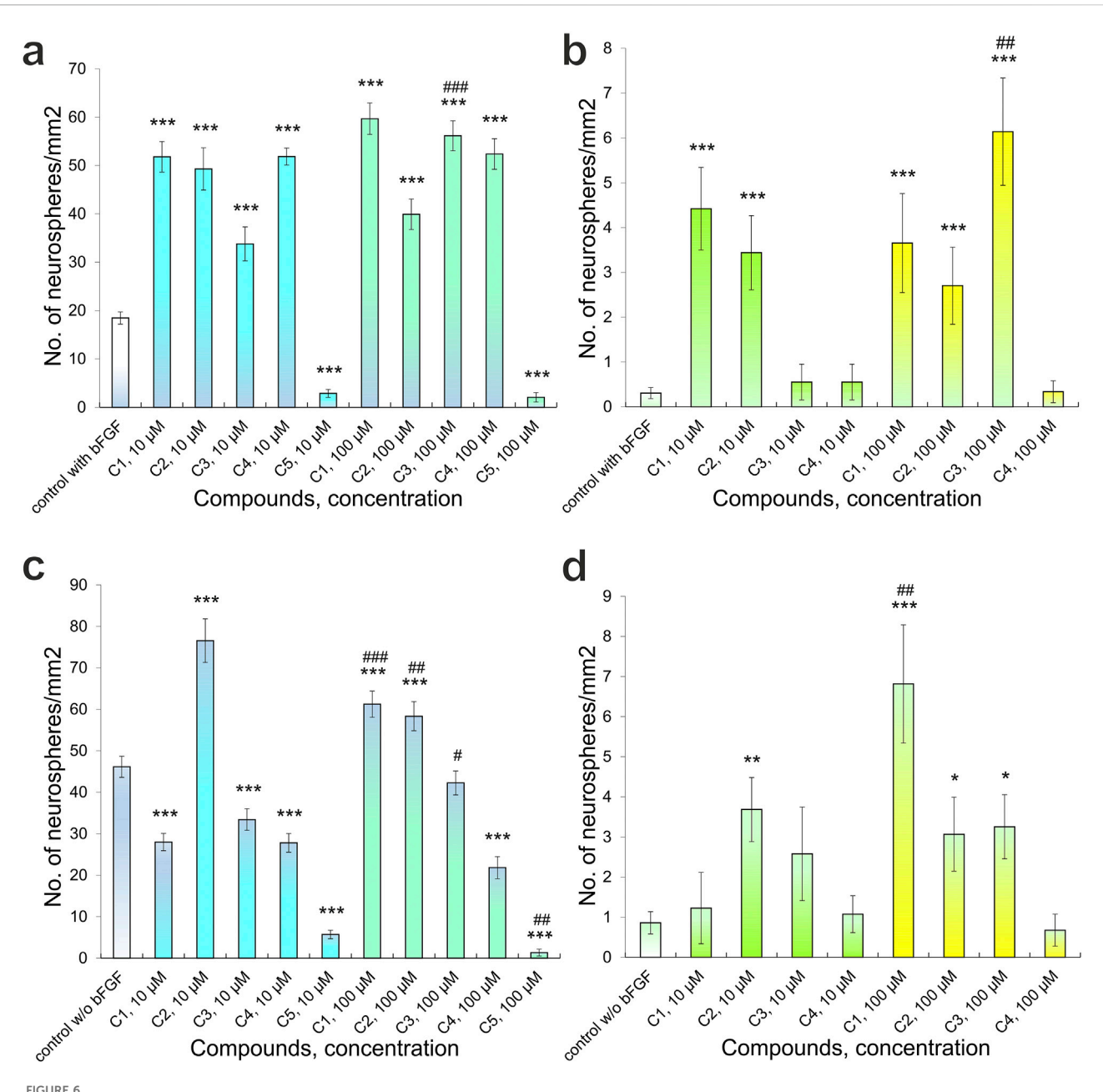


FIGURE 6
Quantitative analysis of primary adhesive neurospheres that form in the presence of Compounds (C1-C5): (a) the number of neurospheres < 50 μ m in diameter, culture conditions with bFGF; (b) the number of neurospheres > 50 μ m in diameter, culture conditions with bFGF; (c) the number of neurospheres < 50 μ m in diameter, culture conditions without bFGF; (d) the number of neurospheres > 50 μ m in diameter, culture conditions without bFGF. P-values derived from the Kruskal-Wallis test, the results are shown as mean \pm SEM; *p < 0.05, **p < 0.01 and ***p < 0.001 *versus* control without bFGF (c,d); #p < 0.05, ##p < 0.01 and ##p < 0.001 *versus* different concentrations of one's compound.

Cultivation conditions influenced the formation of primary adhesive neurospheres. Specifically, in control cultures receiving bFGF supplementation, we observed the formation of 18.48 \pm 1.26 neurospheres with a diameter less than 50 μm and 0.31 \pm 0.12 neurospheres with a diameter greater than 50 μm per mm² (n = 47) (Figures 4a,b, 6a,b). When 10 μM and 100 μM C1-C4 were added to the culture medium, the number of neurospheres with a diameter of <50 μm significantly increased: 51.79 \pm 3.16 (n = 16) (p < 0.001), 49.30 \pm 4.36 (n = 17) (p < 0.001), 33.77 \pm 3.53 (n = 17) (p < 0.001), 51.85 \pm 1.75 (n = 18) (p < 0.001) and 59.68 \pm

 $3.25~(n=16)~(p<0.001), 39.91\pm3.16~(n=17)~(p<0.001), 56.15\pm3.10~(n=17)~(p<0.001), 52.37\pm3.16~(n=18)~(p<0.001)~per mm^2~respectively~(Figures~4c,e,~6a). However, the addition of C5 at concentrations of 10 <math display="inline">\mu M$ and 100 μM significantly reduced neurosphere formation to $2.85\pm0.83~(n=15,~p<0.001)$ and $2.06\pm0.98~(n=15,~p<0.001)~per~mm^2,$ respectively (Figure 6a). Similarly, varying concentrations of C3 also significantly impacted neurosphere formation (p<0.001); specifically, increasing C3 concentrations led to a substantially greater number of neurospheres with a diameter <50 μm (Figure 6a).

The addition of compounds C1, C2, C3, and C4 to bFGF-supplemented experimental cultures led to an increase in neurospheres larger than 50 μm in diameter. The observed counts per mm² were: for C1, 4.42 \pm 0.92 (10 μM , n = 16, p < 0.001) and 3.45 \pm 0.83 (100 μM , n = 17, p < 0.001); for C2, 0.55 \pm 0.40 (10 μM , n = 17) and 0.55 \pm 0.40 (100 μM , n = 18); for C3, 3.65 \pm 1.10 (10 μM , n = 16, p < 0.01) and 2.70 \pm 0.86 (100 μM , n = 17, p < 0.05); and for C4, 6.14 \pm 1.20 (10 μM , n = 17, p < 0.001) and 0.34 \pm 0.24 (100 μM , n = 18) (Figure 6b). The addition of C5 to the culture medium, at various tested concentrations, did not result in the formation of neurospheres with a diameter greater than 50 μm . Separately, for neurospheres smaller than 50 μm , higher concentrations of C3 led to a significant increase in their number (p < 0.01), consistent with previous observations of C3's effect on these smaller neurospheres (Figure 6b).

Culturing NSCs with no added bFGF resulted in formation of primary adhesive neurospheres of various diameters in control cultures, namely, diameter of $<50 \mu m - 46.14 \pm 2.55 (n = 35)$ and >50 μ m - 0.86 \pm 0.28 (n = 35) per mm² (Figures 6c,d). Addition of 10 µM C1 significantly decreased the number of neurospheres with a diameter of $<50 \mu m - 27.99 \pm 2.09 (n = 16) (p < 0.001) per$ mm2, while adding 100 µM C1 significantly increased the number of neurospheres to 61.22 ± 3.16 (n = 18) (p < 0.001) per mm² (Figure 6c). Moreover, a significant difference (p < 0.001) in the number of neurospheres formed was observed when C1 of different concentrations was added: increased C1 concentration led to significantly greater number of neurospheres with a diameter of <50 µm (Figure 6c). On the other hand, both experimental concentrations, 10 μM and 100 μM , of C2 in the culture medium led to an increase in the number of neurospheres with a diameter of <50 μ m: 76.53 \pm 5.25 (n = 15) (p < 0.001) and 58.33 \pm 3.50 (n = 16) (p < 0.001) per mm², respectively (Figures 4d, 6c). Apart from that, increasing concentration of C2 led to a significant (p < 0.01) decrease in the number of neurospheres with a diameter of <50 µm, although this figure was substantially higher than in the control cultures (Figures 4, 6c). C3-C5 at concentrations of 10 μ M and 100 μ M contributed to a decrease in the number of neurospheres with a diameter of $<50 \mu m$: $33.43 \pm 2.58 (n = 19) (p < 10)$ 0.001), 27.81 \pm 2.24 (n = 17) (p < 0.001), 5.71 \pm 1.01 (n = 14) (p < 0.001) to 42.24 ± 2.88 (n = 17), 21.83 ± 2.67 (n = 18) (p < 0.001), 1.35 ± 0.83 (n = 16) (p < 0.001) per mm², respectively (Figures 4f,h, 6c). Although when 100 μM C3 was added to the culture medium, a significant (p < 0.05) increase in the number of neurospheres of a given diameter was observed, compared to cultures cultivated with 10 µM C3, however, this indicator was still lower than the control (Figure 6c). Increasing the concentration of C5 led to a significant (p < 0.01) decrease in the number of neurospheres with a diameter of <50 μ M (Figure 6c).

The addition of C1-C5 to the NSC culture medium also affected the formation of neurospheres larger than 50 μm in diameter. Specifically, C1-C3 at both 10 μM and 100 μM concentrations increased the number of these larger neurospheres: 1.23 \pm 0.89 (n = 16), 3.68 \pm 0.80 (n = 15) (p < 0.01), 2.58 \pm 1.17 (n = 19) Ta 6.81 \pm 1.47 (n = 18) (p < 0.001), 3.07 \pm 0.92 (n = 16) (p < 0.05), 3.25 \pm 0.80 (n = 17) (p < 0.05) per mm², respectively (Figure 6d). Notably, a significant difference (p < 0.01) in the number of neurospheres (>50 μm) was observed with varying C1 concentrations; higher C1 concentrations resulted in a significantly greater number of these

larger neurospheres (Figure 5d). Adding 10 μM C4 to the culture medium slightly increased the number of neurospheres >50 μm to 1.07 ± 0.46 per mm^2 (n = 17). In comparison, 100 μM C4 led to a decrease to 0.67 \pm 0.40 per mm^2 (n = 18) (Figure 6d). Regardless of the presence or absence of bFGF, C5 at all tested concentrations inhibited the formation of neurospheres with a diameter exceeding 50 μm .

In this study, we also performed immunocytochemical evaluation of NSCs cultured under different conditions. NSCs grown under standard conditions (with bFGF) maintained their undifferentiated state, as indicated by Nestin, and showed significant proliferative potential, as indicated by Ki-67 (Figure 7a). In these standard cultures (with bFGF), we also observed a small number of MAP-2-positive neurons and α - and $\beta(III)$ -tubulin-positive elements of the neuroblast cytoskeleton, indicating the onset of differentiation in individual cells or within neurospheres (Figure 8a). In contrast, culturing NSCs without bFGF led to a significant decrease in Ki-67-positive cells (reduced proliferation) and a substantial increase in differentiation into neurons, as evidenced by the markers as mentioned above (Figures 7d, 8d).

Following the addition of C1-C4 at 10 µM and 100 µM, we observed a decrease in total cell number and a significant reduction in NSC proliferation, accompanied by an increase in cells expressing neuronal markers MAP-2, α-tubulin, and β(III)-tubulin (Figures 7a-c). Significant neuronal differentiation was also apparent within neurospheres. It is interesting to note that when cultivating NSCs (+bFGF) with C2 (at different concentrations), a decrease in proliferative activity according to the Ki-67 marker was observed, along with a significant increase in the number of neurospheres, which mainly contained differentiated cells - neurons (Figures 7b,c, 8b,c). Notably, in bFGF-free medium, 10 µM C4 significantly increased the number of proliferating NSCs compared to the control (Figure 7e). This indicates that C4 at this specific concentration can support NSC proliferation independently of exogenous bFGF. Conversely, the presence of C4 significantly inhibited both neuronal differentiation and neurosphere formation compared to the control cultures (Figure 8e).

In summary, short-term (48 h) culture with C1–C4 allows NSCs to maintain viability and other stem cell characteristics. These compounds were also found to affect NSC proliferation and the formation of primary adhesive neurospheres. Additionally, the presence of C1, C2, C3, and C4 led to noticeable qualitative changes in the α -tubulin and $\beta(III)$ -tubulin components of the cellular cytoskeleton's microtubules. Therefore, we conclude that C1–C4 directly influence NSC proliferation and differentiation into neurons without exhibiting cytotoxicity at the tested concentrations. In contrast, C5 was found to be toxic to NSC cultures at the concentrations used.

Conclusion

Despite the binding site's challenging geometry, we developed an effective high-throughput screening model using a sophisticated combination of structural and ligand-based approaches. The on-thefly parameter tuning proved beneficial, allowing for rapid and accurate analysis of large databases and ensuring procedural reproducibility that accommodated changes at each iteration.

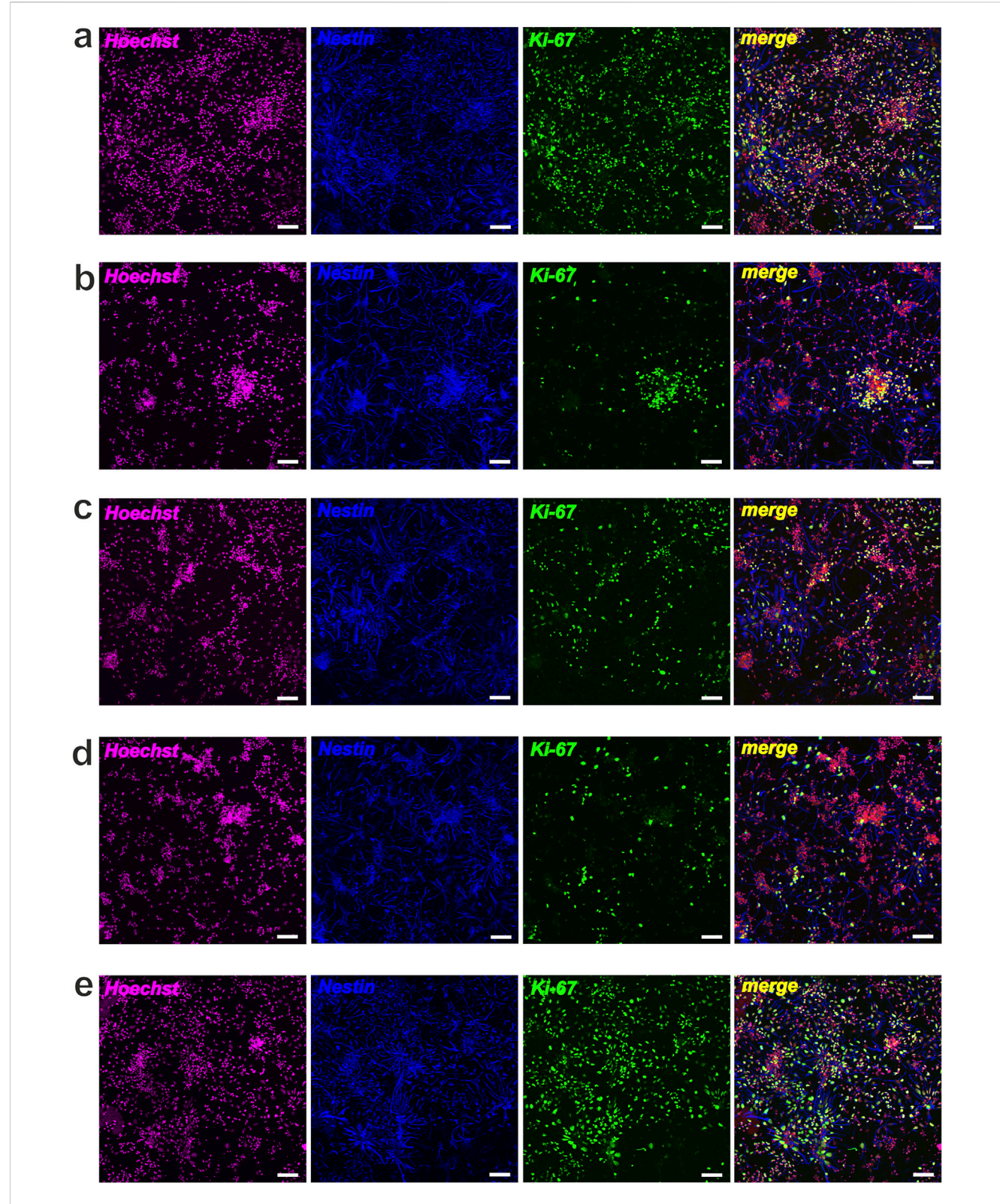


FIGURE 7 NSCs proliferative activity after cultivation (48 h) with Compounds (C1-C5). Representative confocal images of NSCs stained for Hoechst (magenta), Nestin (blue) and Ki-67 (green): (a) control, NSCs + bFGF; (b) NSCs + bFGF+10 μ M C2; (c) NSCs + bFGF+100 μ M C2; (d) control, NSCs w-o bFGF; (e) NSCs+10 μ M C4; scale bars = 50 μ m.

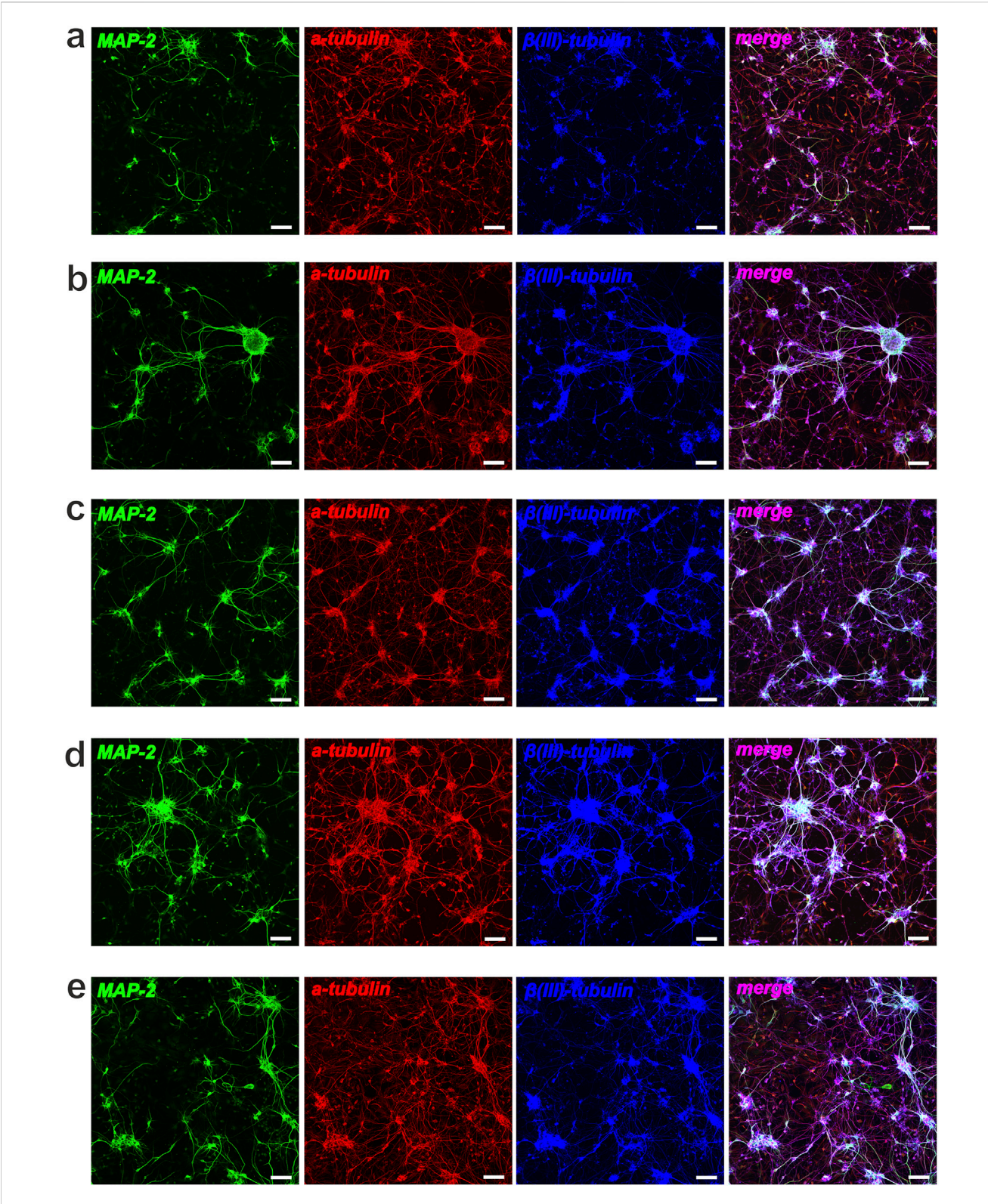


FIGURE 8
Neuronal differentiation of NSCs after cultivation (48 h) with Compounds (C1-C5). Representative confocal images of NSCs stained for MAP-2 (green), α -tubulin (red) and β (III)-tubulin (blue): (a) control, NSCs + bFGF; (b) NSCs + bFGF+10 μ M C2; (c) NSCs + bFGF+100 μ M C2; (d) control, NSCs w-o bFGF; (e) NSCs+10 μ M C4; scale bars = 50 μ m.

Consequently, despite the lack of specific reference inhibitors, our molecular screening identified a set of compounds with potential activity. Structural analysis of aTAT1 complexes with experimentally validated ligands allowed us to propose three pharmacophore hypotheses for specific inhibition and to develop the most functional docking model for aTAT1. Importantly, shortterm cultivation of neural stem cells with the novel molecules (C1, C2, C3, C4) demonstrated that the NSCs maintained their viability and other characteristic stem cell properties. We observed that C1, C2, C3, and C4 added to the culture medium influence NSC proliferation and the formation of primary adhesive neurospheres. Furthermore, these compounds induced qualitative and quantitative changes in the cytoskeletal microtubule proteins αtubulin and β (III)-tubulin. Thus, our findings indicate that the new molecules (C1-C4) directly impact NSC proliferation and differentiation (especially towards neurons) and are not cytotoxic at the concentrations used. The obtained data will be used to refine the pharmacophore model for improved accuracy and to facilitate further screening of the Enamine (https://enamine.net.ua/) and Life Chemicals (https://lifechemicals.com) commercial databases.

This study contributes to a project aiming to identify indirect modulators of the nociceptive nervous system. Despite the separate development of a method for studying pain-related ion channels (Platonov et al., 2024a; Platonov et al., 2024b), the enhanced αTAT1 inhibitory activity suggests a future point of convergence for indirectly blocking the pain cascade.

Data availability statement

The original contributions presented in the study are included in the article/supplementary material, further inquiries can be directed to the corresponding author.

Ethics statement

Animals were used by the protocols approved by the Animal Care and Use Committee at Bogomoletz Institute of Physiology (Kyiv, Ukraine) and the Law of Ukraine on the protection of experimental animals (N3447-IV, 21.02.2006).

Author contributions

OR: Investigation, Writing – original draft, Data curation, Formal Analysis, Methodology. AR: Investigation, Methodology, Writing – original draft, Conceptualization, Validation, Writing – review and editing. MS: Conceptualization, Formal Analysis, Methodology, Writing – original draft. DS: Conceptualization, Formal Analysis, Project administration, Writing – original draft. EB: Investigation, Visualization, Writing – original draft. MP: Investigation, Methodology, Resources, Writing – original draft. YB: Project administration, Supervision, Writing – review and editing. PK: Funding

acquisition, Project administration, Software, Writing - original draft.

Funding

The author(s) declare that financial support was received for the research and/or publication of this article. The work was supported by the National Research Foundation of Ukraine (https://nrfu.org. ua/) under the project "Enzymes of posttranslational modifications of microtubules proteins, as targets for excitability inhibition of primary nociceptive neurons of peripheral nervous system," State Registration No 0120U104883. The study was carried out using CCDC GOLD software, kindly pro-vided by the Cambridge Crystallographic Data Center (CCDC) as part of the Frank H. Allen International Research and Education Program(FAIRE) grant ID: 21554 and the capacities of the Grid Cluster of the Institute of Food Biotechnology and Genomics of the National Academy of Sciences of Ukraine and the virtual organization CSLabGrid (http://ifbg.org.ua/en/cslabgrid).

Acknowledgments

We express our sincere gratitude to the Company Inte: Ligand GmbH (www.inteligand.com) for the license for the LigandScout software package.

Conflict of interest

Authors BE and MP were employed by Enamine Ltd.

The remaining authors declare that the research was conducted in the absence of any commercial or financial relationships that could be construed as a potential conflict of interest.

Generative AI statement

The author(s) declare that no Generative AI was used in the creation of this manuscript.

Any alternative text (alt text) provided alongside figures in this article has been generated by Frontiers with the support of artificial intelligence and reasonable efforts have been made to ensure accuracy, including review by the authors wherever possible. If you identify any issues, please contact us.

Publisher's note

All claims expressed in this article are solely those of the authors and do not necessarily represent those of their affiliated organizations, or those of the publisher, the editors and the reviewers. Any product that may be evaluated in this article, or claim that may be made by its manufacturer, is not guaranteed or endorsed by the publisher.

References

Adasme, M. F., Linnemann, K. L., Bolz, S. N., Kaiser, F., Salentin, S., Haupt, V. J., et al. (2021). PLIP 2021: expanding the scope of the protein-ligand interaction profiler to DNA and RNA. *Nucleic Acids Res.* 49 (W1), W530–W534. doi:10.1093/nar/gkab294

Aguilar, A., Becker, L., Tedeschi, T., Heller, S., Iomini, C., and Nachury, M. V. (2014). A-tubulin K40 acetylation is required for contact inhibition of proliferation and cell-substrate adhesion. *Mol. Biol. Cell* 25 (12), 1854–1866. doi:10.1091/mbc.E13-10-0609

Coombes, C. E., Saunders, H. A. J., Mannava, A. G., Johnson-Schlitz, D. M., Reid, T. A., Parmar, S., et al. (2020). Non-enzymatic activity of the α -tubulin acetyltransferase aTAT limits synaptic bouton growth in neurons. *Curr. Biol.* 30 (4), 610–623. doi:10.1016/j.cub.2019.12.022

Dan, W., Gao, N., Li, L., Zhu, J. X., Diao, L., Huang, J., et al. (2018). α-Tubulin acetylation restricts axon overbranching by dampening microtubule plus-end dynamics in neurons. *Cereb. cortex (New York, N. Y. 1991)* 28 (9), 3332–3346. doi:10.1093/cercor/hbx225

Dybkova, N., Wagner, S., Backs, J., Hund, T. J., Mohler, P. J., Sowa, T., et al. (2014). Tubulin polymerization disrupts cardiac β -adrenergic regulation of late INa. *Cardiovasc. Res.* 103 (1), 168–177. doi:10.1093/cvr/cvu120

Ferreira de Freitas, R., Harding, R. J., Franzoni, I., Ravichandran, M., Mann, M. K., Ouyang, H., et al. (2018). Identification and structure-activity relationship of HDAC6 zinc-finger ubiquitin binding domain inhibitors. *J. Med. Chem.* 61 (10), 4517–4527. doi:10.1021/acs.jmedchem.8b00258

Friedmann, D. R., Aguilar, A., Fan, J., Nachury, M. V., and Marmorstein, R. (2012). Structure of the α -tubulin acetyltransferase, α TAT1, and implications for tubulin-specific acetylation. *Proc. Natl. Acad. Sci. U. S. A.* 109 (48), 19655–19660. doi:10.1073/pnas.1209357109

Fu, Y., Xiao, S., Hong, T., and Shaw, R. M. (2015). Cytoskeleton regulation of ion channels. *Circulation* 131 (8), 689–691. doi:10.1161/circulationaha.115.015216

Goswami, C., Kuhn, J., Heppenstall, P. A., and Hucho, T. (2010). Importance of non-selective cation channel TRPV4 interaction with cytoskeleton and their reciprocal regulations in cultured cells. *PLoS One* 5 (7), e11654. doi:10.1371/journal.pone.0011654

Han, S. K., Song, J. D., Noh, Y. S., and Noh, B. (2007). Role of plant CBP/p300-like genes in the regulation of flowering time. *Plant J.* 49 (1), 103-114. doi:10.1111/j.1365-313X.2006.02939.x

Hsu, N. Y., Pathak, N., Chen, Y. T., Hsu, Y. C., and Yang, J. M. (2021). Pharmacophore anchor models of ATAT1 to discover potential inhibitors and lead optimization. *Comput. Biol. Chem.* 93, 107513. doi:10.1016/j.compbiolchem.2021. 107513

Huang, J., Rauscher, S., Nawrocki, G., Ran, T., Feig, M., de Groot, B. L., et al. (2017). CHARMM36m: an improved force field for folded and intrinsically disordered proteins. *Nat. methods* 14 (1), 71–73. doi:10.1038/nmeth.4067

Iuzzolino, A., Pellegrini, F. R., Rotili, D., Degrassi, F., and Trisciuoglio, D. (2024). The α -tubulin acetyltransferase ATAT1: structure, cellular functions, and its emerging role in human diseases. *Cell Mol. Life Sci.* 81 (1), 193. doi:10.1007/s00018-024-05227-x

Jan, E., and Kotov, N. A. (2007). Successful differentiation of mouse neural stem cells on layer-by-layer assembled single-walled carbon nanotube composite. *Nano Lett.* 7 (5), 1123–1128. doi:10.1021/nl0620132

Janke, C., and Magiera, M. M. (2020). The tubulin code and its role in controlling microtubule properties and functions. *Nat. Rev. Mol. Cell Biol.* 21 (6), 307–326. doi:10. 1038/s41580-020-0214-3

Karpov, P., Brytsun, V. M., Demchuk, O. M., Pydiura, N. O., Ozheredov, S. P., Samofalova, D. A., et al. (2015). High-throughput screening of new antimitotic compounds based on CSLabGrid virtual organization. *Sci. Innov.* 11 (1), 85–93. doi:10.15407/scine11.01.085

Karpov, P., Demchuk, O. M., Brytsun, V. M., Lytvyn, D. I., Pydiura, N. O., Rayevsky, A. V., et al. (2016). New imidazole inhibitors of mycobacterial FtsZ: the way from high-throughput molecular screening in grid up to *in vitro* verification. *Sci. Innov.* 12 (3), 43–55. doi:10.15407/scine12.03.043

Laskowski, R. A., and Swindells, M. B. (2011). LigPlot+: multiple ligand-protein interaction diagrams for drug discovery. *J. Chem. Inf. Model.* 51 (10), 2778–2786. doi:10.1021/ci200227u

Liu, N., Xiong, Y., Li, S., Ren, Y., He, Q., Gao, S., et al. (2015). New HDAC6-mediated deacetylation sites of tubulin in the mouse brain identified by quantitative mass spectrometry. *Sci. Rep.* 5, 16869. doi:10.1038/srep16869

López-López, E., Naveja, J. J., and Medina-Franco, J. L. (2019). DataWarrior: an evaluation of the open-source drug discovery tool. *Expert Opin. Drug Discov.* 14 (4), 335–341. doi:10.1080/17460441.2019.1581170

Platonov, M., Maximyuk, O., Rayevsky, A., Hurmach, V., Iegorova, O., Naumchyk, V., et al. (2024a). 4-(Azolyl)-Benzamidines as a novel chemotype for ASIC1a inhibitors. *Int. J. Mol. Sci.* 25 (7), 3584. doi:10.3390/ijms25073584

Platonov, M., Maximyuk, O., Rayevsky, A., Iegorova, O., Hurmach, V., Holota, Y., et al. (2024b). Integrated workflow for the identification of new GABA(A) R positive allosteric modulators based on the *in silico* screening with further *in vitro* validation.

Case study using Enamine's stock chemical space. Mol. Inf. 43 (2), e202300156. doi:10. $1002/\min f.202300156$

Rakhshani, H., Dehghanian, E., and Rahati, A. (2019). Enhanced GROMACS: toward a better numerical simulation framework. *J. Mol. Model* 25 (12), 355. doi:10.1007/s00894-019-4232-z

Rayevsky, A., Sharifi, M., Samofalova, D., Karpov, P., and Blume, Y. (2016). 3D structure prediction of histone acetyltransferase proteins of the MYST family and their interactome in *Arabidopsis thaliana*. *J. Mol. Model.* 22, 256. doi:10.1007/s00894-016-3103-0

Rayevsky, A. V., Sharifi, M., Samofalova, D. A., Karpov, P. A., and Blume, Y. B. (2019). Structural and functional features of lysine acetylation of plant and animal tubulins. *Cell Biol. Int.* 43 (9), 1040–1048. doi:10.1002/cbin.10887

Rayevsky, A., Bulgakov, E., Sharifi, M., Samofalova, D., Ozheredov, D., Karpov, P., et al. (2023). In silico induced effect of N- ϵ -lysine acetylation on microtubule stability and subsequent interaction of microtubule-associated proteins. Cell Biol. Int. 47 (9), 1547–1557. doi:10.1002/cbin.12052

Rayevsky, A., Bulgakov, E., Blume, R., Novozhylov, D., Stykhylias, M., Ozheredov, S., et al. (2025). Lysine acetylation of plant α-tubulins: scaling up the local effect to large system transformations. *Proteins Struct. Funct. Bioinforma.* 93, 1848–1861. doi:10.1002/prot.26846

Rayevsky, A., Bulgakov, E., Stykhylias, M., Ozheredov, S., Spivak, S., and Blume, Y. (2025). Structural flexibility and shape similarity contribute to exclusive functions of certain Atg8 isoforms in the autophagy process. *Mol. Inf.* 44 (47), e202500025. doi:10.1002/minf.70004

Rybachuk, O., Kopach, O., Pivneva, T., and Kyryk, V. (2019). Isolation of Neural Stem Cells from the embryonic mouse hippocampus for *in vitro* growth or engraftment into a host tissue. *Bio Protoc.* 9 (4), e3165. doi:10.21769/BioProtoc.3165

Samofalova, D. O., Karpov, P. A., Raevsky, A. V., and Blume, Y. B. (2019). Protein phosphatases potentially associated with regulation of microtubules, their spatial structure reconstruction and analysis. *Cell Biol. Int.* 43 (9), 1081–1090. doi:10.1002/cbin.10810

Sánchez-Fernández, R., Sánchez-Temprano, A., Esteban-Gómez, D., and Pazos, E. (2023). Probing tyrosine nitration with a small Tb(III) -metallopeptide. *Chembiochem a Eur. J. Chem. Biol.* 24 (13), e202300072. doi:10.1002/cbic.202300072

Sardar, P., Kumar, A., Bhandari, A., and Goswami, C. (2012). Conservation of tubulin-binding sequences in TRPV1 throughout evolution. *PLoS One* 7 (4), e31448. doi:10.1371/journal.pone.0031448

Studer, G., Rempfer, C., Waterhouse, A. M., Gumienny, R., Haas, J., and Schwede, T. (2020). QMEANDisCo-distance constraints applied on model quality estimation. *Bioinformatics* 36 (6), 1765–1771. doi:10.1093/bioinformatics/btz828

Stykhylias, M., Rayevsky, O., and Blume, Y. (2024). Plant histone deacetylases: their classification and inhibitor search. *Cytol. Genet.* 58, 385–394. doi:10.3103/S0095452724050116

Topalidou, I., Keller, C., Kalebic, N., Nguyen, K. C., Somhegyi, H., Politi, K. A., et al. (2012). Genetically separable functions of the MEC-17 tubulin acetyltransferase affect microtubule organization. *Curr. Biol.* 22 (12), 1057–1065. doi:10.1016/j.cub.2012.03.066

Ustinova, K., Novakova, Z., Saito, M., Meleshin, M., Mikesova, J., Kutil, Z., et al. (2020). The disordered N-terminus of HDAC6 is a microtubule-binding domain critical for efficient tubulin deacetylation. *J. Biol. Chem.* 295 (9), 2614–2628. doi:10.1074/jbc. RA119.011243

UniProt Consortium (2025). UniProt: the universal protein knowledgebase in 2025. Nucleic Acids Res. 53 (D1), D609–D617. doi:10.1093/nar/gkae1010

Wolber, G., and Langer, T. (2005). LigandScout: 3-D pharmacophores derived from protein-bound ligands and their use as virtual screening filters. *J. Chem. Inf. Model.* 45 (1), 160–169. doi:10.1021/ci049885e

Wolber, G., Dornhofer, A. A., and Langer, T. (2006). Efficient overlay of small organic molecules using 3D pharmacophores. *J. Comput. Aided Mol. Des.* 20 (12), 773–788. doi:10.1007/s10822-006-9078-7

Wong, C. O., Chen, K., Lin, Y. Q., Chao, Y., Duraine, L., Lu, Z., et al. (2014). A TRPV channel in Drosophila motor neurons regulates presynaptic resting Ca2+ levels, synapse growth, and synaptic transmission. *Neuron* 84 (4), 764–777. doi:10.1016/j.neuron.2014. 09 030

Wu, K., Wang, L., Chen, Y., Pirooznia, M., Singh, K., Wälde, S., et al. (2018). GCN5L1 interacts with α TAT1 and RanBP2 to regulate hepatic α -tubulin acetylation and lysosome trafficking. *J. Cell Sci.* 131 (22), jcs221036. doi:10.1242/jcs.221036

Xiong, Z., Zhao, S., Mao, X., Lu, X., He, G., Yang, G., et al. (2014). Selective neuronal differentiation of neural stem cells induced by nanosecond microplasma agitation. *Stem Cell Res.* 12 (2), 387–399. doi:10.1016/j.scr.2013.11.003

Zardecki, C., Dutta, S., Goodsell, D. S., Lowe, R., Voigt, M., and Burley, S. K. (2022). PDB-101: educational resources supporting molecular explorations through biology and medicine. *Protein Sci.* 31 (1), 129–140. doi:10.1002/pro.4200